Naval Research Laboratory

Computation of Forces on a Rotating WindSat Reflector

RAVI RAMAMURTI

Center for Reactive Flow and Dynamical Systems
Laboratory for Computational Physics and Fluid Dynamics

December 20, 2002

REPORT DOCUMENTATION PAGE

Public reporting burden for this collection of information is estimated to average 1 hour per response, including the time for reviewing instructions, searching existing data sources, gathering and maintaining the data needed, and completing and reviewing this collection of information. Send comments regarding this burden estimate or any other aspect of this collection of information, including suggestions for reducing this burden to Department of Defense, Washington Headquarters Services, Directorate for Information Operations and Reports (0704-0188), 1215 Jefferson Davis Highway, Suite 1204, Arlington, VA 22202-4302. Respondents should be aware that notwithstanding any other provision of law, no person shall be subject to any penalty for failing to comply with a collection of information if it does not display a currently valid OMB control number. **PLEASE DO NOT RETURN YOUR FORM TO THE ABOVE ADDRESS.**

1. REPORT DATE (DD-MM-YYYY)	2. REPORT TYPE	3. DATES COVERED (From - To)
December 20, 2002	NRL Memorandum Report	

4. TITLE AND SUBTITLE	5a. CONTRACT NUMBER
Computation of Forces on a Rotating WindSat Reflector	5b. GRANT NUMBER 64-K267-L-3
	5c. PROGRAM ELEMENT NUMBER
6. AUTHOR(S)	5d. PROJECT NUMBER
	5e. TASK NUMBER
Ravi Ramamurti	5f. WORK UNIT NUMBER

7. PERFORMING ORGANIZATION NAME(S) AND ADDRESS(ES)	8. PERFORMING ORGANIZATION REPORT NUMBER
Naval Research Laboratory 4555 Overlook Avenue, SW Washington, DC 20375-5320	NRL/MR/6410--02-8654

9. SPONSORING / MONITORING AGENCY NAME(S) AND ADDRESS(ES)	10. SPONSOR / MONITOR'S ACRONYM(S)
Commander COMSPAWARSYSCOM 4301 Pacific Highway Code 01-4 San Diego, CA 92110-3127	11. SPONSOR / MONITOR'S REPORT NUMBER(S)

12. DISTRIBUTION / AVAILABILITY STATEMENT

Approved for public release; distribution is unlimited.

13. SUPPLEMENTARY NOTES

14. ABSTRACT

The flow over the rotating WindSat reflector is computed. The primary aim of this effort is to compute the lifting force that is normal to the reflector and the moments it produces about the center of the rotating system. This force and the moments produced cannot be compensated otherwise. The unstructured mesh-based flow solver *FEFLO* is used to compute this flow in the frame of reference rotating with the reflector. The flow solver is first validated against test problems with known analytical solutions. *FEFLO* is then applied to compute the flow over the reflector. Effects of presence of the trusses supporting the reflector are also studied. The results obtained will serve to provide an upper bound on the forces that will be experienced by the rotating system, and therefore in the calculation of the jitter angle of the WindSat reflector.

15. SUBJECT TERMS

WindSat; Rotating frame; Incompressible flow; Unstructured grid

16. SECURITY CLASSIFICATION OF:			17. LIMITATION OF ABSTRACT	18. NUMBER OF PAGES	19a. NAME OF RESPONSIBLE PERSON Ravi Ramamurti
a. REPORT	b. ABSTRACT	c. THIS PAGE	UL	19	19b. TELEPHONE NUMBER (include area code) (202) 767-0608
Unclassified	Unclassified	Unclassified			

Table of Contents

Table of contents

Computation of Forces on a Rotating Wheeled Reflector

INTRODUCTION

A satellite based wind speed and direction detecting system called the WindSat has been developed by NRL. The inner reflector of the WindSat system rotates and it rotates in the Fresnel quasi-optics interferometrial resonator.

INCOMPRESSIBLE FLOW SOLVER

The governing equations employed are the incompressible Navier-Stokes equations in Arbitrary Lagrangian Eulerian (ALE) formulation. They are written as

$$(1)$$

$$(2)$$

$$(3)$$

Computation of Forces on a Rotating WindSat Reflector

INTRODUCTION

A satellite based wind speed and direction detecting system called the WindSat has been developed by NRL. The main reflector of the WindSat system rotates and is connected to the Coriolis spacecraft via an interface and stationary platform. Any unbalanced force produced by the rotating antenna would result in a wobble in the entire spacecraft. It is therefore critical to assess the forces produced by the rotating antenna and counterbalance appropriately. In order to measure imbalance of forces, the reflector assembly is tested with the test bed spinning in the clockwise direction. The direction of rotation is then reversed and the forces are measured. From these two tests, the imbalance of forces in the circumferential direction and its moments about the spin axis can be obtained and corrected by adding counterbalancing weights. The force normal to the reflector, a lift force, and its moments about the axis of rotation can not be determined from these two tests. The aim of this effort is to computationally obtain the lift force on the rotating reflector.

INCOMPRESSIBLE FLOW SOLVER

FEFLO is a finite element-based incompressible flow solver based on simple, low-order elements. The simple elements enable the flow solver to be as fast as possible reducing the overhead in building element matrices, residual vectors etc. The governing equations are written in Arbitrary Lagrangian Eulerian form which enables simulation of flow with moving bodies. For high Reynolds number flow cases, the mesh requirement is met by employing arbitrary semi-structured grids close to wetted surfaces and wakes. The full details of the flow solver, the rigid body motion and adaptive remeshing are given by Ramamurti et al.[1] and are summarized next.

The governing equations employed are the incompressible Navier-Stokes equations in Arbitrary Lagrangian Eulerian (ALE) formulation. They are written as

$$\frac{D\mathbf{v}}{Dt} + \mathbf{v}_a \cdot \nabla \mathbf{v} + \nabla p = \nabla \cdot \sigma \tag{1a}$$

$$\frac{D\mathbf{v}}{Dt} = \frac{\partial \mathbf{v}}{\partial t} + \mathbf{w} \cdot \nabla \mathbf{v} \tag{1b}$$

$$\nabla \cdot \mathbf{v} = 0 \tag{2}$$

Here p denotes the pressure, $\mathbf{v}_a = \mathbf{v} - \mathbf{w}$, the advective velocity vector (flow velocity $\mathbf{v}$ minus mesh velocity $\mathbf{w}$), and the material derivative is with respect to the mesh velocity $\mathbf{w}$. Both the pressure p and the stress tensor σ have been normalized by the (constant) density ρ, and are discretized in time using an implicit time stepping procedure. It is important for the flow solver to be able to capture the unsteadiness of a flow field. The present flow solver is built as time-accurate from the onset, allowing local timestepping as an option. The resulting expressions are subsequently discretized in space using a Galerkin procedure with linear tetrahedral elements. In order to be as fast as possible, the overhead in building element matrices, residual vectors, etc. should be kept to a minimum. This requirement is met by employing simple, low-order elements that have all the variables (u,v,w,p) at the same location. The resulting matrix systems are solved iteratively using a preconditioned gradient algorithm (PCG). The flow solver has been

successfully evaluated for both 2-D and 3-D, laminar and turbulent flow problems by Ramamurti et al.[2,3]

In a frame of reference rotating with an angular velocity Ω, Eq. (1a) can be written as

$$\frac{D\mathbf{v}}{Dt} + \mathbf{v}_a \cdot \nabla\mathbf{v} + \nabla p = \nabla \cdot \sigma - 2\Omega \times \mathbf{v} - \Omega \times (\Omega \times \mathbf{v}) \tag{3}$$

Compared to the stationary frame of reference, we have additional source terms from the Coriolis and centrifugal forces.

COMPUTATIONAL RESULTS

The *FEFLO* flow solver in the rotating frame of reference was first validated using two test problems. The first test problem is the flow near a rotating disk. The flow in the vicinity of the disk is validated with exact solution. This is essential for computing forces and moments on a reflector-like geometry where the pressure on the surface and the velocity in the vicinity of the disk are the most important parameters. The second test case is that of flow between two rotating cylinders. The purpose of this test is to validate the computations in the rotating frame of reference.

Flow near a rotating disk

The first test problem is the flow near a rotating disk shown in Fig. 1. A flat plate rotates about an axis perpendicular to its plane with a uniform angular velocity ω, in a fluid otherwise at rest. An exact solution of the Navier-Stokes equations is possible for this case and is given by Schlichting[4]. Introducing a dimensionless distance from the wall $\zeta = z\sqrt{\dfrac{\omega}{\nu}}$ and using the following assumptions for the radial, circumferential and axial velocity components and pressure,

$$u = r\omega \ F(\zeta), \ v = r\omega \ G(\zeta), \ w = \sqrt{\nu\omega}H(\zeta) \text{ and}$$
$$p = p(z) = \rho\nu\omega \ P(\zeta) , \tag{4}$$

Eq. (1) can be written as a system of four simultaneous ordinary differential equations for the functions F, G, H and P:

$$2F + H' = 0$$
$$F^2 + F'H - G^2 - F'' = 0$$
$$2FG + HG' - G'' = 0 \tag{5a}$$
$$P' + HH' - H'' = 0 .$$

The boundary conditions for this system can be obtained from the no slip conditions at the wall and no flow far away from the plate and are:

at $\zeta = 0$: $F = 0, \ G = 1, \ H = 0, \ P = 0$ and
at $\zeta = \infty$: $F = 0, \ G = 0.$ \hspace{1cm} (5b)

Equation 5 was solved numerically and the velocity components were then computed using Eq.(4).

The *FEFLO* flow solver was then used to solve the flow past this configuration as shown in Fig. 2. Here the flat plate was of a finite diameter of 1 and the far-field boundaries were set to be at 5. The computed velocities along a line at z= 0.4, shown by the dotted line in Fig 2, were compared to the exact solution of Eq. (5), and are shown in Fig. 3. There is excellent agreement with the theory close to the wall. The radial and axial components, u and w respectively, are in exact agreement. There is a small discrepancy in the tangential component (*v*) away from the flat plate. This is due to the nearness of the outer boundaries and also due to the fact that the spinning disk is of finite radius and the edge effect cannot be neglected. Figure 4a-d show the distribution of the velocity components and the pressure along *xz* plane passing through the center of the disk. The radial (*u*) and circumferential (*v*) velocity components distributions are anti-symmetric about the *y* axis, Fig. 4a and b. The effect of the edge and the outer boundary can be seen in these contours near the edge of the disk for small values of *z* and the effect spreads away from the wall. The effect of the outer boundary is most pronounced in the axial (*w*) component of the velocity, Fig 4c. The pressure distribution shown in Fig. 4d depends on the distance from the wall for very small values of *z*, consistent with the boundary layer theory. However, away from the wall a radial pressure gradient is present which is produced to the effect of the edge.

Flow between rotating cylinders

In order to validate the *FEFLO* flow solver in rotating frame of reference, the flow between two concentric rotating cylinders was chosen. An exact solution of the Navier-Stokes equation is given by Schlichting[4]. In this example, the two concentric cylinders move at different but steady rotational speeds. The inner and outer radii are r_1 and r_2, and move with angular velocities ω_1 and ω_2, respectively. The circumferential velocity v is given by

$$v(r) = \frac{1}{r_2^2 - r_1^2}\left[r\left(\omega_2 r_2^2 - \omega_1 r_1^2\right) - \frac{r_1^2 r_2^2}{r}\left(\omega_2 - \omega_1\right)\right] \tag{6a}$$

For the special case when the inner cylinder is rotating and the outer one is at rest, the velocity is

$$v(r) = \omega_1 r_1\left(\frac{r_1}{r}\right)\left(\frac{r_2^2 - r^2}{r_2^2 - r_1^2}\right) . \tag{6b}$$

The configuration for this computation is shown in Fig. 5a with the inner radius of 1 and outer radius of 3. Computations were performed in both stationary and rotating frames of reference with the rotational velocity of the inner cylinder $\omega = 60$ rpm. Figure 6 shows the comparison of the circumferential velocity between the cylinders for both of these computations with the exact solution (Eq. 6b), and the agreement is excellent. It was found that the solution in the rotating frame of reference converged very slowly mainly due to the explicit treatment of Coriolis force terms. Figures 7a show the circumferential velocity distribution on an *xz* plane and is anti-symmetric about the origin. The pressure and the magnitude of velocity on a $z =$ constant (=0.5) plane is shown in Figs. 7b and 7c, respectively and are axisymmetric.

WindSat Reflector

Having successfully validated the flow solver for the two cases, the *FEFLO* was applied to compute the flow past the WindSat reflector. First, the reflector was considered without the supporting trusses. The reason being, that the trusses would decelerate the flow and hence, the

case without the trusses would yield a conservative estimate of the lift and drag forces generated on the reflector. The geometry of the WindSat reflector was obtained from Code 8230 and is shown in Fig. 8. The reflector is obtained from the intersection of a parabolic surface, $x^2 = 4\,Cz$, with a cylinder of 71.6 in diameter. The axis of the cylinder is offset from the axis of the parent parabola by 50 in. The center of the chord in the plane of the resultant parabolic section is then allowed to rotate about an axis offset by 20in. For computations, this geometry is set in a rotating frame of reference with the outer boundaries at 15 ft from the axis of rotation. The boundary conditions on this far field are prescribed velocities rotating in the direction opposite to the rotation of the reflector.

The incompressible flow solver described above was employed to compute the steady inviscid flow about this configuration. From our past experience, an inviscid flow model is sufficient to obtain the correct lift forces, if the flow over this configuration is not separated. The effect of viscosity will increase the drag forces, in the circumferential direction. The effect of this drag force on the unbalanced moments can be obtained by reversing the rotational direction. The rotational speed, ω, of the reflector was first set to 60 rpm. The steady state flow over this configuration was obtained in 2000 time steps. The force on the reflector surface and the moment about the origin were obtained by integrating the pressure distribution on its surface. The computed force components for this case are $f_x = -0.99$ lbs, $f_y = 3.398$ lbs and $f_z = 0.58$ lbs. The moments about the local origin shown in Fig. 8 are $M_x = -6.01$ ft-lbs, $M_y = -3.185$ ft-lbs and $M_z = 8.112$ ft-lbs.

Figures 9a and b show the pressure distribution on the top and bottom surfaces of the reflector. It can be seen that regions of high pressure exist on the edge of the reflector in the $-z$ direction and almost half of the bottom surface in the $+z$ direction. Figures 10a and b show the distribution of the magnitude of velocity on the two surfaces. On the top surface, the velocity distribution is almost uniform, but on the bottom surface we see a high velocity region near $+x$ axis or the leading edge and a small recirculation region in the $-x$ direction or the trailing edge of the reflector. Figure 11 shows the velocity vectors on the bottom surface. Again, the small recirculation region is clearly seen in Fig. 11b.

Next, the flow past this configuration was obtained with the reflector rotating in the counter clockwise direction at 60 rpm. The force and moment components obtained for this case are $f_x = -0.99$ lbs, $f_y = 3.382$ lbs and $f_z = -0.58$ lbs, and $M_x = 5.97$ ft-lbs, $M_y = 3.172$ ft-lbs and $M_z = 8.024$ ft-lbs, respectively. This shows that the force in the y direction remains almost the same with the force in the circumferential direction opposite to the previous case, as expected. Another computation was performed to assess the forces at a reduced rotational speed of $\omega = 30$ rpm. For this case, the computed force and moment components are $f_x = -0.248$ lbs, $f_y = 0.849$ lbs and $f_z = 0.1637$ lbs, $M_x = -1.51$ ft-lbs, $M_y = 0.8$ ft-lbs and $M_z = 2.032$ ft-lbs, respectively. Comparing the magnitude of the forces to the case of $\omega = 60$ rpm, it is clear that the force components are reduced by a factor of 4. This is to be expected as the forces are proportional to the square of the velocity, and the rotational speed was decreased by a factor of 2.

Effect Of Viscosity

In order to study the effect of viscosity on the forces developed on the reflector, the viscous flow over the reflector was computed. The Reynolds number (Re) for this flow based on the maximum rotational tip velocity and the diameter of the reflector is 1.2×10^6. A turbulent flow past the reflector was computed using a Smagorinsky[5] turbulence model. Figure 12 shows the

convergence history for the forces for both the inviscid and viscous turbulent flow simulations. The converged forces and moments are $f_x = -1.25$ lbs, $f_y = 3.96$ lbs and $f_z = -0.664$ lbs, and $M_x = -6.199$ ft-lbs, $M_y = -3.394$ ft-lbs and $M_z = 8.345$ ft-lbs, respectively. All the force components increased in magnitude compared to the inviscid prediction. The increase in drag forces f_x and f_z are to be expected. The increase in lift force f_y is due to the higher peak pressure on the bottom surface of 1.43×10^{-3} psi gauge (Fig. 13b) for the viscous case compared to a peak value of 1.27×10^{-3} psi gauge for the inviscid case although the pressure distribution on the top surface is quite similar (Fig. 13a). The increased peak pressure on the bottom surface is due to the presence of the leading edge vortex that can be seen in the velocity vectors on the $y=0$ plane shown in Fig. 14.

Effect Of The Presence Of Trusses
The supporting trusses were added to the reflector from the CAD model given in terms of IGES files from Code 8230. These IGES descriptions were converted to *fecad* format using the GridTool[6] software. This CAD model was modified so that it is suitable for CFD calculations by matching various members of the trusses and eliminating very small gaps in the structure (Fig. 15). A volume mesh was generated for this configuration consisting of 106,310 boundary points, 526,636 total points and 2,805,589 tetrahedral elements. Inviscid and viscous flows past this configuration were computed for the configuration rotating at $\omega = 60$ rpm in the clockwise direction about the y-axis.

The convergence history of the forces is shown in Fig. 16. It is clear that the differences between inviscid and viscous cases are negligible. The converged forces and moments about the origin shown in Fig. 15, for the inviscid case are $f_x = -0.303$ lbs, $f_y = 1.189$ lbs and $f_z = 0.56$ lbs, $M_x = -2.66$ ft-lbs, $M_y = -3.50$ ft-lbs and $M_z = 6.30$ ft-lbs, respectively; for the viscous case, the forces and moments are $f_x = -0.302$ lbs, $f_y = 1.084$ lbs and $f_z = 0.641$ lbs, $M_x = -2.69$ ft-lbs, $M_y = -3.84$ ft-lbs and $M_z = 5.74$ ft-lbs, respectively. Comparing these forces for the case without the trusses, we find that the drag force in the x-direction (f_x) is reduced in magnitude, from -0.99 lbs to -0.3lbs, due to the influence of the keel structure above the reflector. The drag force in the z-direction (f_z) is nearly unchanged. The lift force (f_y) on the other hand is reduced considerably from 3.95 lbs to 1.08 lbs. To understand the reason for this reduced lift, the pressure distributions on the reflector surfaces for the inviscid and viscous cases are plotted and are shown in Figs. 17 and 18 respectively. Comparing this pressure distribution to the case without the trusses (Fig. 9 and Fig. 13), we see that the peak pressure on the bottom surface in the case without the trusses is much higher and extends over a larger area. Also, the region of low pressure (blue) on the bottom surface in the case with the trusses is much larger leading to a lower lift force. The influence of the trusses on the pressure can be clearly seen on the top surface.

The moments about the origin shown in Fig. 15 are computed for the case of the standalone reflector. The local origin is displaced from the origin of the entire system (reflector and trusses) mainly in the y direction. The displacements in the x and y directions are $0.86''$ and $82.9''$, respectively. Hence, the moments about the origin of the entire system can be computed. For the inviscid case, they are $M_x = -2.001$ ft-lbs, $M_y = -3.226$ ft-lbs and $M_z = 15.231$ ft-lbs, and for the viscous case, $M_x = -1.612$ ft-lbs, $M_y = -3.441$ ft-lbs and $M_z = 17.286$ ft-lbs. The moments about the x- and y-axes are of the same order of magnitude in comparison with the trusses, but the moments about the z-axis differs considerably. This change is due to the partly due to the change

in the f_x and f_y components of the force. The other contribution to the change in M_z arises due to the change in center of pressure. The center of pressure for the reflector was computed for the viscous cases with and without the trusses. For the case without the trusses, the center of pressure was located at $x_p = (30.01'', 70.79'', 16.82'')$. In the case with trusses, the center of pressure was found to be at $x_p = (50.76'', 45.83'', 56.91'')$. The change in the x and y moment arms thus contribute to the majority of the change in the moment component M_z. The forces and moments for all the cases computed were provided to the Spacecraft Engineering Department for computations of the jitter angle of the rotating system.

The flow between the reflector and the base of the supporting trusses is shown in Fig. 19. Particle traces near the trailing edge of the reflector are shown in Fig. 19a. These particles are released from a rake of rectangular grid of points (shown in light green color in Fig. 19a) whose plane is parallel to the diameter of the reflector and 0.5″ displaced from the edge of the reflector. Using the instantaneous velocity field, the positions of these particles were obtained by integrating the velocity at these points until the length of these traces exceeded a specified length, or the particles ended on a solid boundary, or exited the computational domain. These particles are colored according to the magnitude of velocity (in inches/sec.) at that location. A trailing edge vortex can be seen from the particle traces in Fig. 19a. The flow below the reflector and the base of the supporting truss consists of a region of low velocity fluid. Particles released from just below the reflector, Fig. 19b, show that the values of velocity are in the range of 0 to 80 in s^{-1}. Also, these particles end up on the recirculation region located at the bottom of the reflector. The contours of the magnitude of velocity on the $y=0$ plane also shows that the flow in the region between the reflector and the base is nearly stagnant.

REFERENCES

1. Ramamurti, R., Sandberg, W.C. and Löhner, R., "Simulation of a Torpedo Launch Using a 3-D Incompressible Finite Element Flow Solver and Adaptive Remeshing," AIAA Paper No. 95-0086, January 1995.

2. Ramamurti, R. and Löhner, R., "Evaluation of an Incompressible Flow Solver Based on Simple Elements," *Advances in Finite Element Analysis in Fluid Dynamics*, 1992, FED Vol. 137, Editors: M.N Dhaubhadel et al., *ASME* Publication, New York, pp. 33-42.

3. Ramamurti, R., Löhner, R. and Sandberg, W.C., "Evaluation of Scalable 3-D Incompressible Finite Element Solver," *AIAA Paper* No. 94-0756, 1994.

4. Schlichting, H., *Boundary Layer Theory*, Seventh Edition, McGraw-Hill, New York.

5. Smagorinsky, J., General Circulation Experiments with the Primitive Equations I. The Basic Experiment; *Mon. Weather Rev.*, 91, pp. 99-164, 1963.

6. Samareh, J., "GridTool: A surface Modeling and Grid Generation Tool," Proc. of the workshop on Surface Modeling, Grid Generation, and Related Issues in CFD Solutions, NASA CP-3291, May 1995.
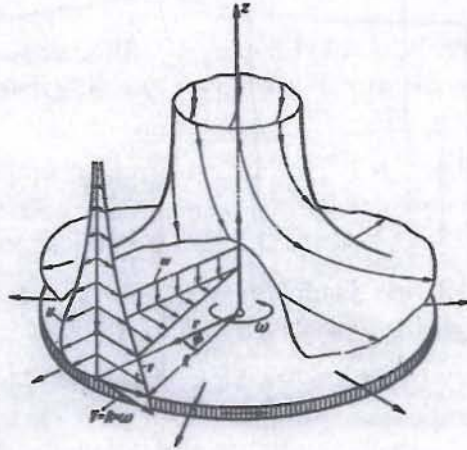
Fig.1. Flow near a rotating disk, from H. Schlichting.
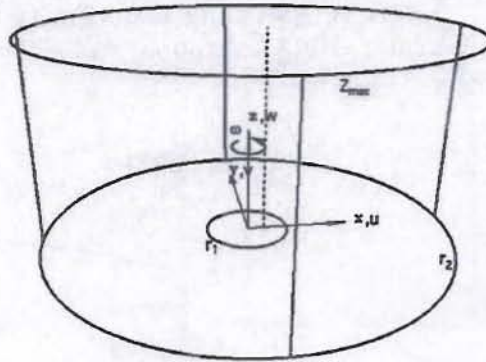
Fig. 2. Computational domain for flow near a rotating disk,
$\omega=60$ rpm, $r_1 = 1.0$, $r_2 = 5.0$ and $z_{max} = 5$.
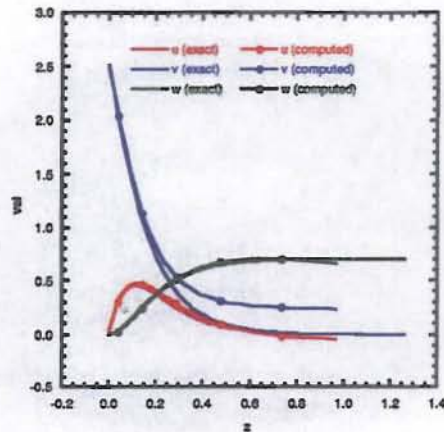
Fig. 3. Comparison of velocity components with the exact solution.
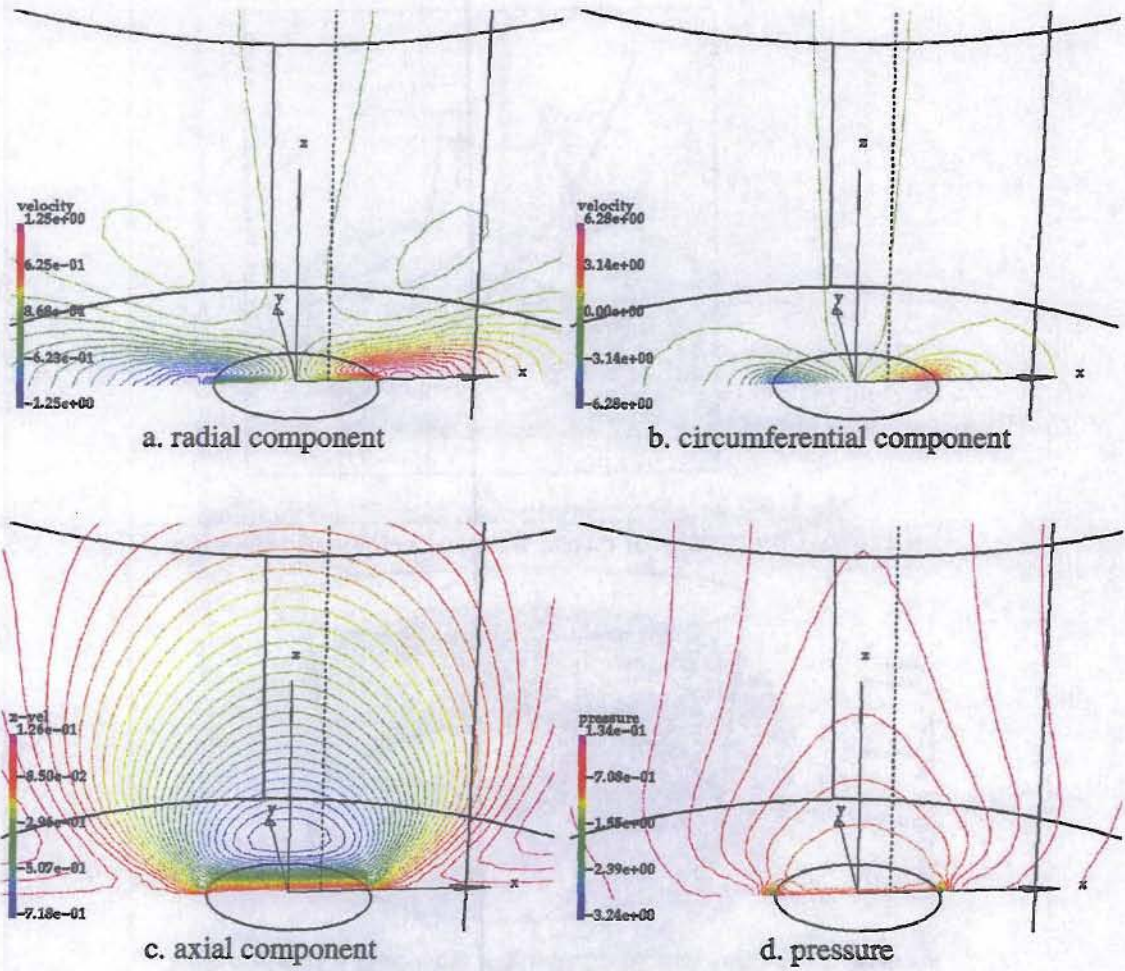
Fig. 4. Velocity and pressure distribution on *y*=0 plane for flow near a rotating disk, ω=60 rpm.
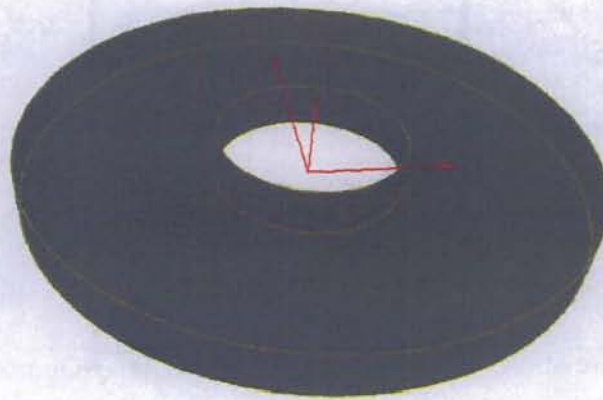
Fig. 5. Flow between two concentric rotating cylinders, inner radius $r_1 = 1$, outer radius $r_2 = 3$.
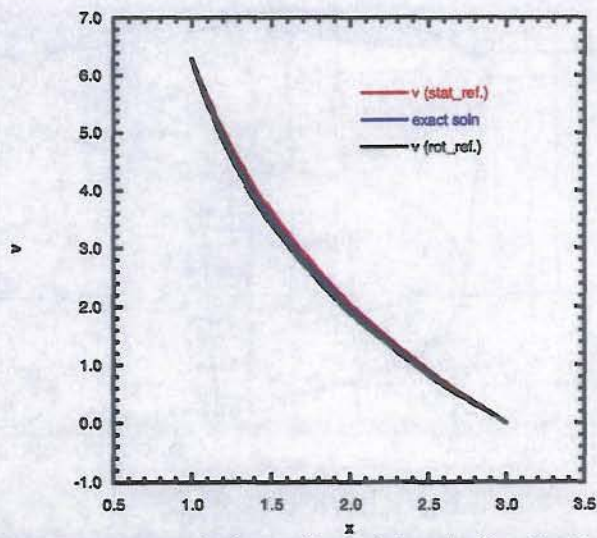
Fig. 6. Comparison of circumferential velocity distribution.
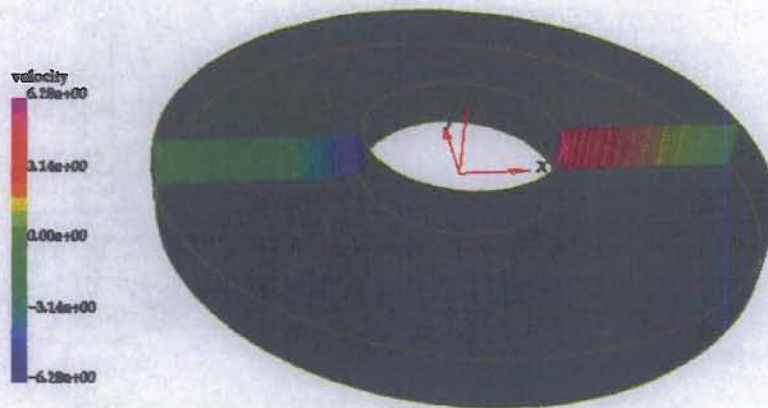
a. circumferential velocity
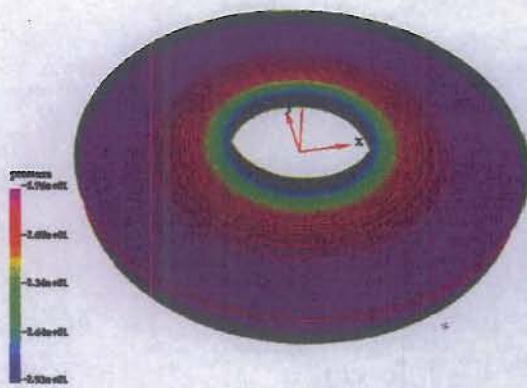
b. pressure
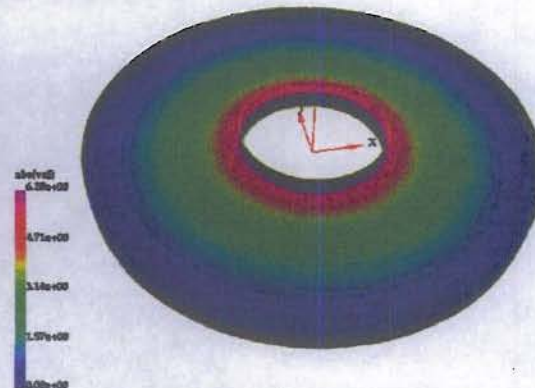
c. magnitude of velocity

Fig. 7. Flow between two concentric rotating cylinders, ω=60 rpm.
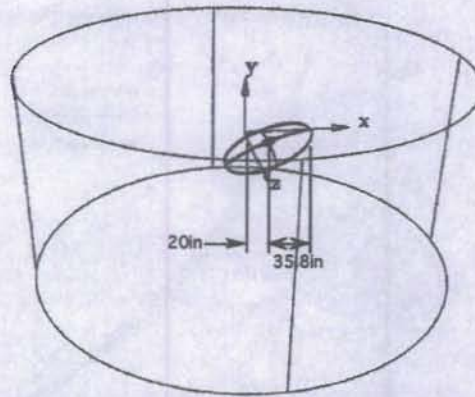
Fig. 8. Computational domain of the WindSat reflector.
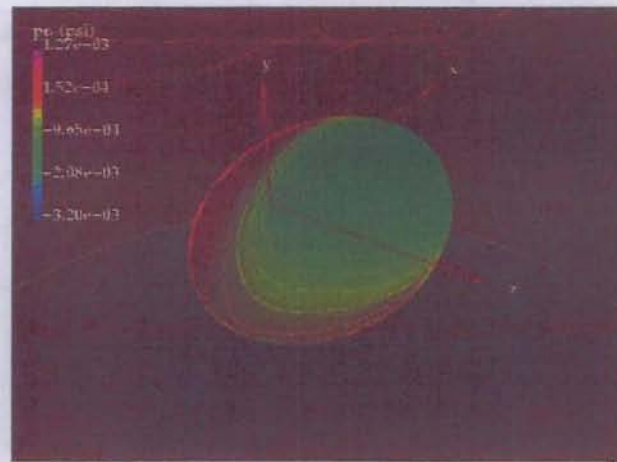
a. top surface
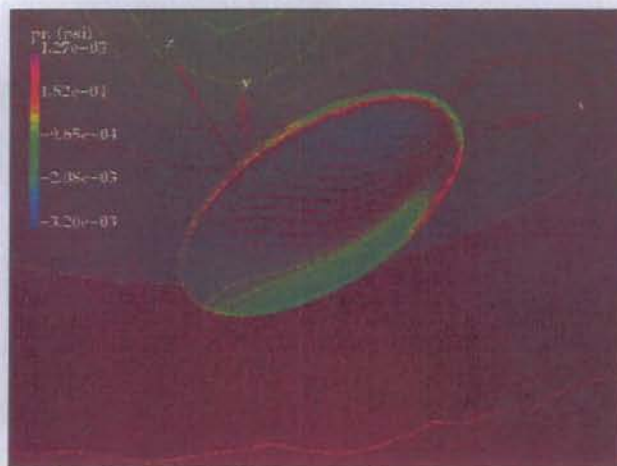
b. bottom surface

Fig. 9. Surface pressure distribution on the reflector, ω = 60 rpm.
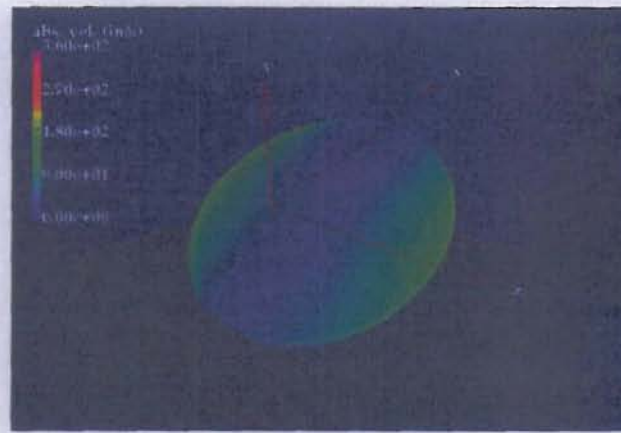
a. top surface
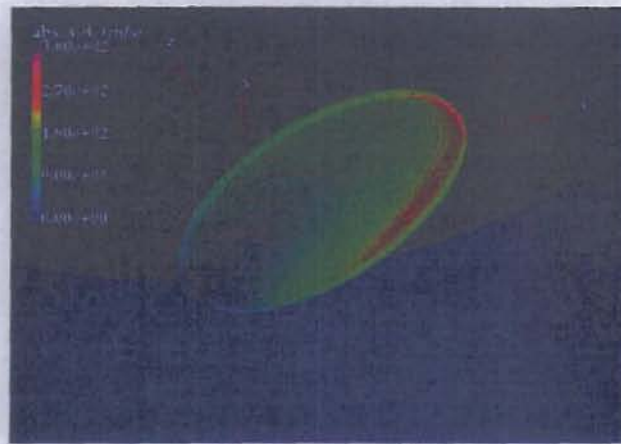
b. bottom surface

Fig. 10. Magnitude of velocity on the surface of the reflector, ω = 60 rpm.
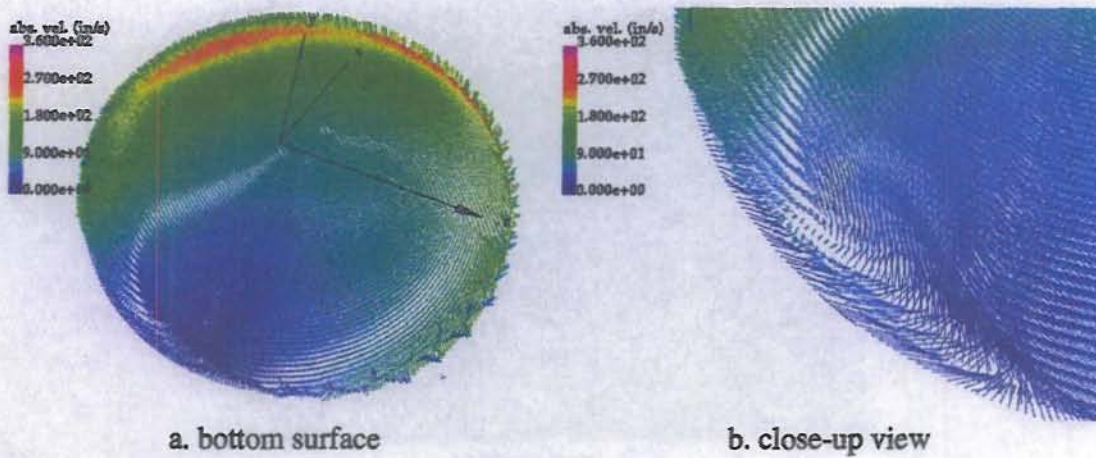
a. bottom surface   b. close-up view

Fig. 11. Velocity vectors on the bottom surface of the reflector, ω = 60 rpm.
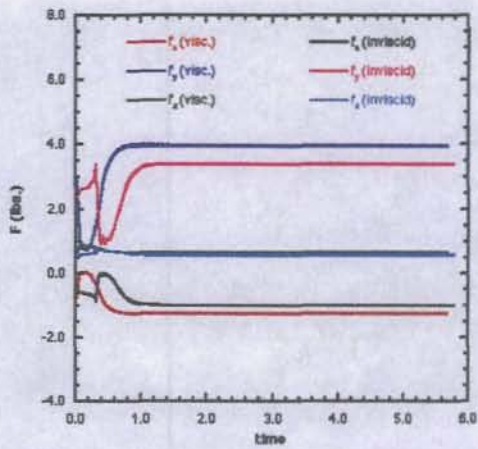
Fig. 12. Convergence history of force components for inviscid and **viscous flows.**
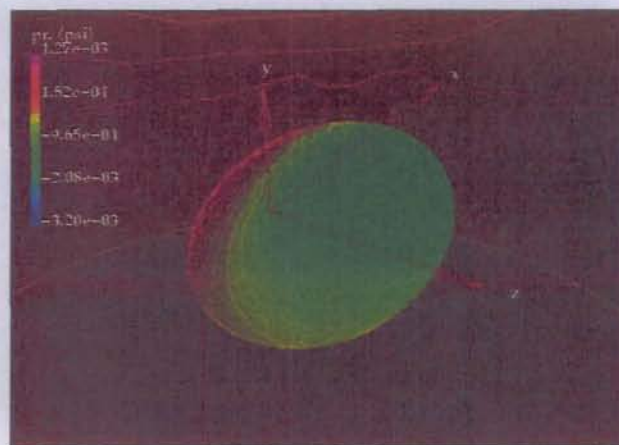
a. top surface
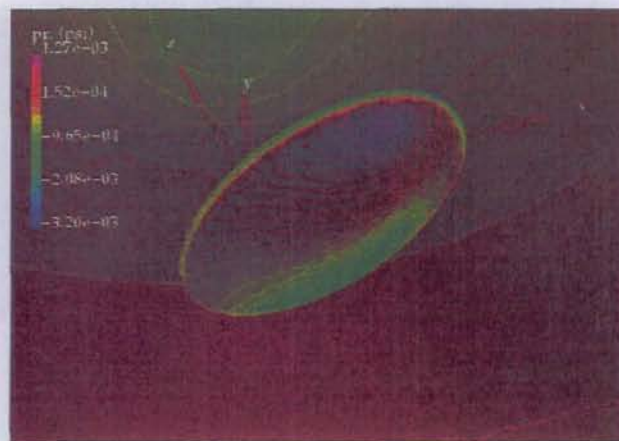
b. bottom surface

Fig. 13. Pressure distribution on the reflector, $Re = 1.2 \times 10^6$.
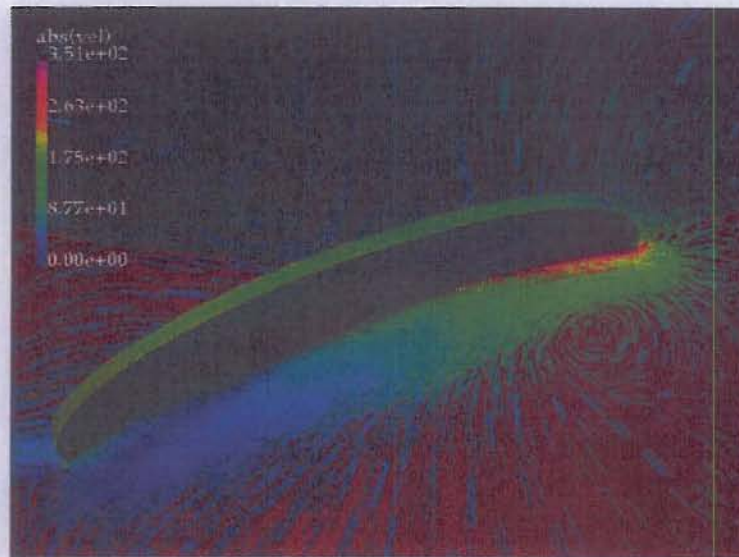
Fig. 14. Velocity vectors on $y = 0$ plane, Re $= 1.2 \times 10^6$.
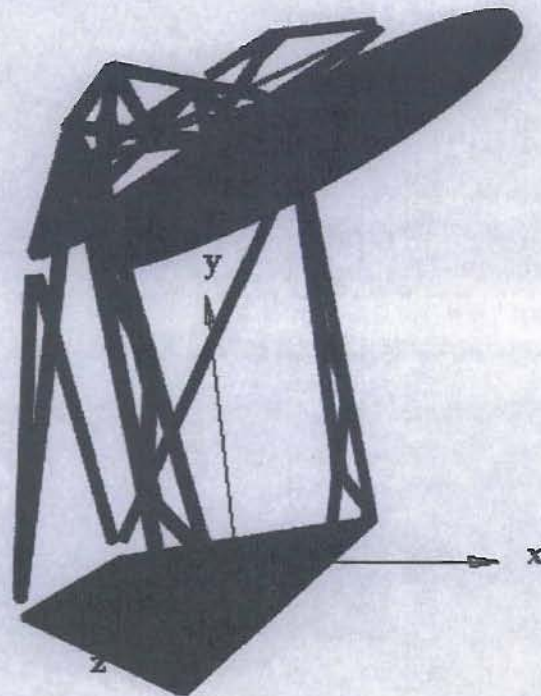

Fig. 15. WindSat reflector with supporting trusses.
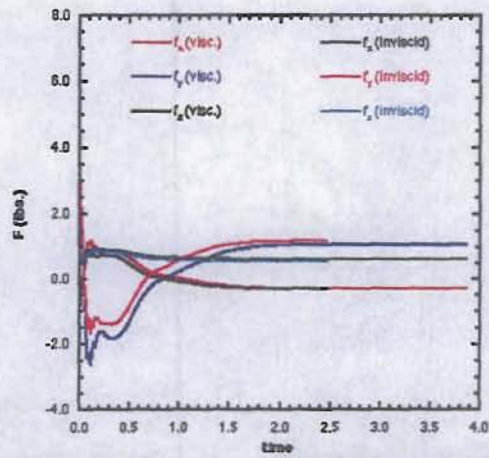
Fig. 16. Convergence history of forces on the reflector in the presence of trusses.
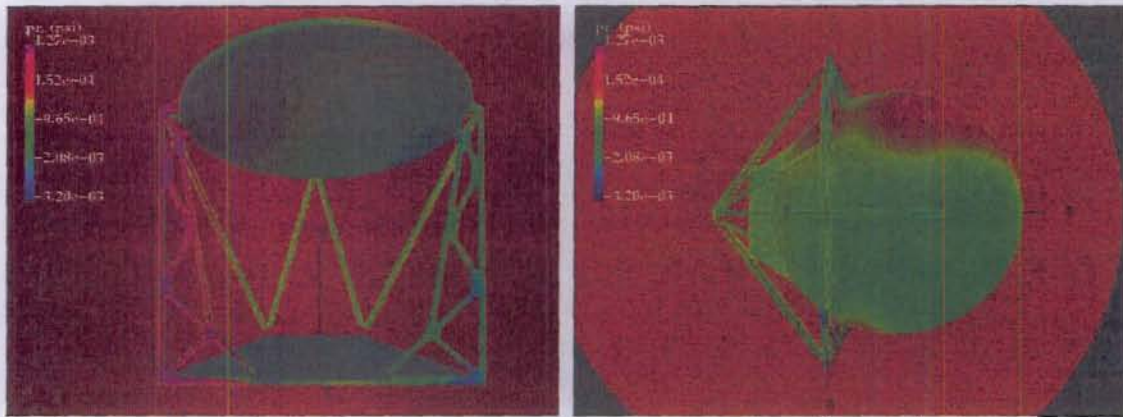
a. front view   b. top view

Fig. 17. Pressure distribution over the WindSat rotating at 60 rpm (inviscid).
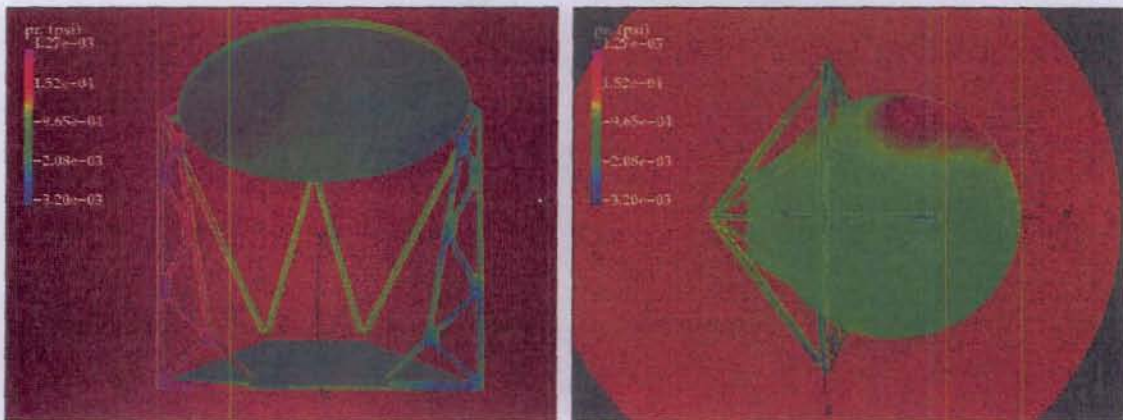
a. front view   b. top view

Fig. 18. Pressure distribution over the WindSat rotating at 60 rpm (viscous).
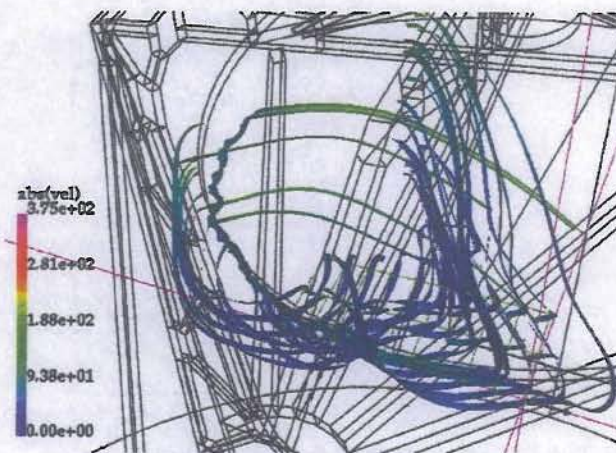
a. particle traces near the trailing edge
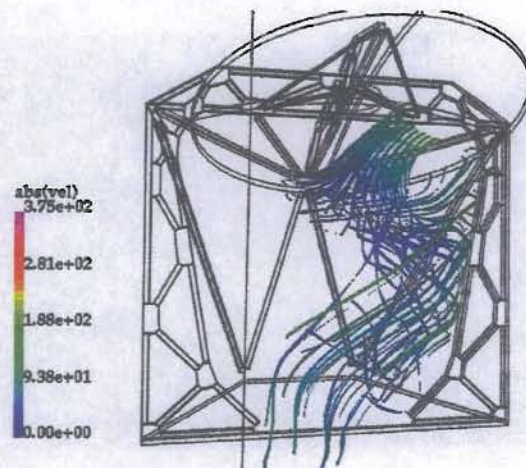
b. particle traces below the reflector
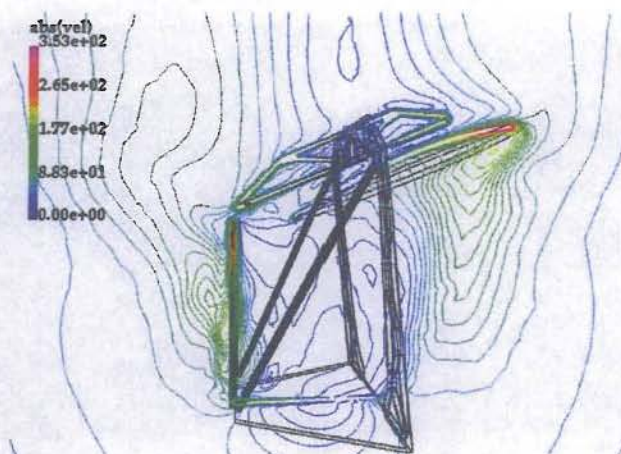

c. magnitude of velocity on $y=0$ plane
Fig. 19. Flow between the reflector and trusses.